

Lifetime measurements in low yrast states and spectroscopic peculiarities in ^{182}Os

A. Harter^{ⓧ,*}, A. Esmaylzadeh[ⓧ], L. Knafla[ⓧ], C. Fransen[ⓧ], F. v. Spee[ⓧ], J. Jolie[ⓧ], M. Ley[ⓧ],
V. Karayonchev[†], J. Fischer[ⓧ], and A. Pfeil[ⓧ]

Universität zu Köln, Mathematisch-Naturwissenschaftliche Fakultät, Institut für Kernphysik, 50937 Cologne, Germany



(Received 2 June 2023; accepted 21 July 2023; published 9 August 2023)

Lifetimes of the low-lying yrast states 2^+ , 4^+ , and 6^+ of the unstable nucleus ^{182}Os were measured using digital fast-timing techniques. The lifetimes of the 4^+ and 6^+ states were determined for the first time. The remeasured value for the lifetime of the 2^+ state was taken into account to evaluate the discrepancy between two inconsistent literature values. The lifetimes and extracted $B(E2)$ values are presented and discussed in terms of collective signatures and transitional phenomena. The $B(E2; 4^+ \rightarrow 2^+)/B(E2; 2^+ \rightarrow 0^+)$ ratio of 1.39(7) supports the interpretation of ^{182}Os as a rigid rotor. This value is discussed in the context of these of the neighboring isotopes and isotones and calculations in the framework of the interacting boson model 1. Additionally, competing influences from the near lying collective deformed region, γ -soft rotors, X(5) symmetry, and neighboring regions of shape coexistence in low excitation states are assumed to influence the structure of the nucleus of interest: The trend of the excitation energies of the γ - and $K^\pi = 0$ -bands in the osmium isotopic chain change remarkably at ^{182}Os . This consideration helps to us delimit and understand the structural transitions in the isotopic and isotonic chains that intersect at ^{182}Os .

DOI: [10.1103/PhysRevC.108.024305](https://doi.org/10.1103/PhysRevC.108.024305)

I. INTRODUCTION

Nuclei with masses $A \approx 180$ in the region around the neutron midshell at $N = 104$ lie at the edge of the strongly deformed region between the neutron shell closures 82 and 126 and proton shell closures 50 and 82. Especially, the isotopes with proton numbers 74 (W), 76 (Os), 78 (Pt), and 80 (Hg) offer a variety of deformation and transition phenomena, e.g., well deformed prolate rotor behavior, X(5) critical point symmetry, γ softness and triaxial phenomena, and shape coexistence near the shell closure $Z = 82$ [1–6]. Figure 1 depicts the nucleus under investigation in this study, ^{182}Os (highlighted by a red circle), positioned precisely at the center of the regions primarily influenced by prolate deformation in the tungsten and hafnium isotopes [7–11], shape coexistence in the mercury and lead isotopes [4], γ softness and triaxiality in the neutron rich osmium and platinum isotopes [12–16], and X(5) critical point symmetry in the lighter osmium isotopes $^{176,178}\text{Os}$ [6,17] and ^{182}Pt [5].

Signatures for collectivity and quadrupole deformation are low excitation energies of the 2^+ states, large $B(E2; 2^+ \rightarrow 0^+)$ values [18], which are connected to the deformation parameter β_2 , and E_{4^+}/E_{2^+} ratios (hereafter $R_{4/2}$) of about 3.3 [18–21]. As Fig. 2 shows, the $R_{4/2}$ ratios of the midshell osmium isotopes lie between the prolate deformed tungsten isotopes with values around the rotational limit of 3.3 and the platinum isotopes, which exhibit γ -soft, triaxial and already spherical signs with $R_{4/2}$ ratios between 2.6 and 2.1. Addition-

ally, the β_2 values of the osmium isotopes with $N = 100$ –112 ($\beta_2 \approx 0.25$ –0.18 [11]) also lie in the descending flank of the β_2 values of the strongly deformed region with masses of $A = 150$ –180 ($\beta_2 < 0.3$ [18]). The dominating phenomena in ^{182}Os are suggested to be collective rotation and moderate quadrupole deformation, especially in comparison with the neighboring isotopes $^{180,184}\text{Os}$ [23–25] and tungsten isotopes $^{178,180,182}\text{W}$, which are suggested to be prolate rotors as well [7]. An excitation energy of the 2^+ state of 126.9 keV, an $R_{4/2} = 3.15$, a reduced transition probability of $B(E2; 2^+ \rightarrow 0^+) = 122(11)$ W.u., and a $\beta_2 = 0.23(1)$ ([26], evaluated values of different works) support this assumption. In the platinum isotopes clear signs of rotor behavior are missing, on the other hand. An ideal rotor shows a $B(E2; 4^+ \rightarrow 2^+)/B(E2; 2^+ \rightarrow 0^+)$ (hereafter $B_{4/2}$) of about $10/7 \approx 1.43$, known as the Alaga rule of the geometric model [19,20]. The osmium isotopic chain is known for notable deviations from the established theoretical limits of 1.43 (rotor) and 2 (vibrator). Especially in the neutron-deficient isotopes very small values of around and smaller than 1 were repeatedly the subject of studies but could not be doubtlessly explained so far [27–29]. As a meeting point of the main influences [strong collectivity, shape coexistence, γ softness, and X(5) critical point symmetry; see Fig. 1], interesting behavior of the level energies in the osmium isotopes around the neutron midshell is observed. Specifically, the investigation of the impact of shape coexistence phenomena, as shown by the occurrence of rotational intruder bands in mercury isotopes [4], and particularly in ^{186}Hg , which is separated from ^{182}Os by only four protons, is an interesting approach.

Only the $B_{4/2}$ ratios of the osmium isotopes 176, 182Os are unknown, hence, the investigation of the transition

*Corresponding author: aharter@ikp.uni-koeln.de

[†]Present address: Argonne National Laboratory, 9700 South Cass Ave., Argonne, IL 60439, USA.

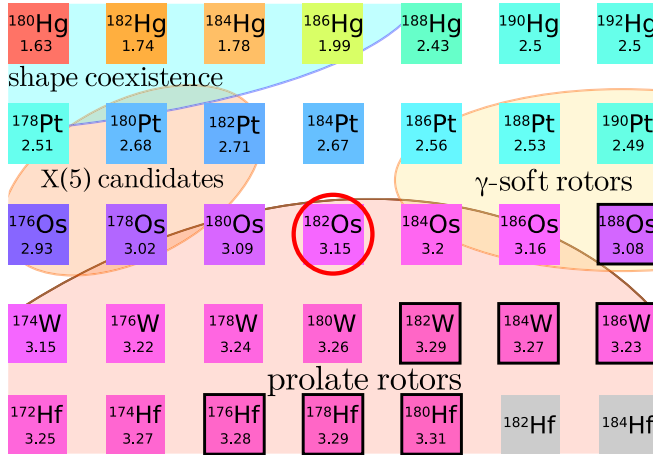


FIG. 1. Even-even isotopes around $A = 180$. The regions of shape coexistence, γ softness, X(5) critical point symmetry, and rotational prolate deformation are roughly identified by elliptical shapes. The nucleus of interest ^{182}Os is indicated by a red circle. The chart is extracted from The colourful nuclide chart by Simpson [22]. The color code of the individual nuclei illustrate the $R_{4/2}$ ratios, which are taken from Ref. [11].

probabilities of the three lowest rotational states in ^{182}Os appears to be a conclusive contribution to delimit the quadrupole deformed region of the rare earths and to understand the transition phenomena in the $A = 180$ region. The lifetimes of these states were expected to be in a fast-timing suitable range and were measured with the recently commissioned digital fast-timing technique [30] using the well established HORUS fast-timing setup [7,31–33].

II. EXPERIMENTAL DETAILS

Excited states in ^{182}Os were populated with the fusion evaporation reaction $^{174}\text{Yb}(^{12}\text{C}, 4n)^{182}\text{Os}$. A ^{174}Yb target of about 4 mg/cm^2 was exposed to an average beam current of 1 p nA with an energy of 66 MeV , which was provided

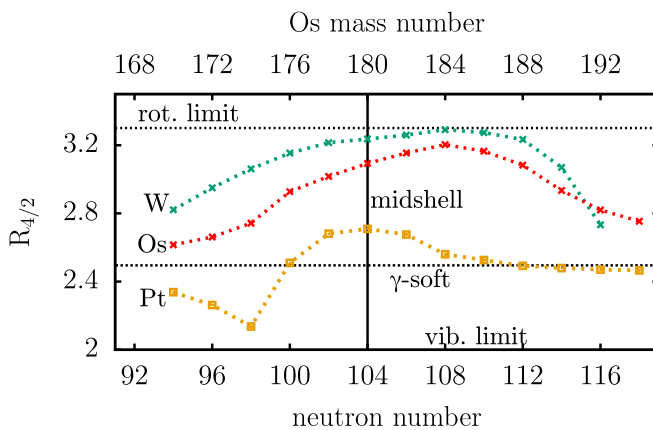


FIG. 2. $R_{4/2}$ ratios of platinum, osmium, and tungsten isotopes. The neutron midshell and the expectation values for rotational and γ -soft limits are indicated in the plot. The lines connecting the data points are meant to guide the eyes. All values are taken from [11].

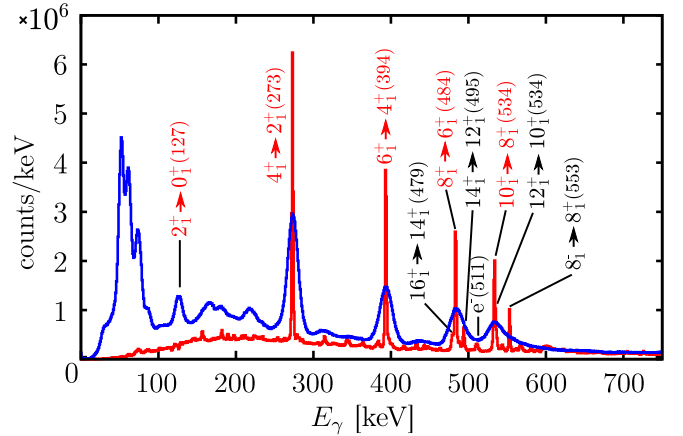


FIG. 3. Spectrum of strongest observed γ rays in coincidence with the $2_1^+ \rightarrow 0_1^+$ ground state transition observed with HPGe detectors for both detector groups: LaBr in blue and HPGe in red. The transitions used for the lifetime analysis are labeled in red. The energy labels are rounded to full keV. The remaining coincidence contribution in the $127 \text{ keV } 2_1^+ \rightarrow 0_1^+$ transition is due to random coincidence. The HPGe detectors were shielded by 2 mm copper and lead plates to prevent high count rates due to intensive x rays in the sub- 100 keV region.

by the Cologne 10 MV FN-Tandem accelerator for about 120 hours . A combined stopper of 196 mg/cm^2 bismuth and 180 mg/cm^2 copper was attached to the target to stop the reaction fragment and the beam to prevent further reactions with the beamline and to enhance the heat dissipation. The yrast band was populated by the fusion evaporation up to the 16^+ state. A negligible population of higher yrast states and states in other excitation bands was detected (see Fig. 3).

The HORUS spectrometer was equipped with ten $\text{LaBr}_3(\text{Ce})$ fast-timing scintillators (LaBr) and eight high-purity germanium detectors (HPGe). The HPGe detectors were shielded against x rays with 2 mm copper and lead plates. Six of the LaBr detectors were surrounded with bismuth germanate (BGO) active Compton suppression shields. The LaBr detector signals were recorded with a fast sampling digitizer of type V1730, manufactured by CAEN S.p.A., with a sampling rate of 500 MS/s and an analog-to-digital converter (ADC) resolution of 14 bits . The module is equipped with an on-board real-time digital interpolating constant fraction discriminator that provides picosecond-level accuracy in time stamps for the fast LaBr detector pulses. The highly accurate time stamps enable the digital fast-timing method [30].

III. DATA ANALYSIS

The expected lifetimes of the 2_1^+ , 4_1^+ , and 6_1^+ states in ^{182}Os were in the time range between 5 ps and some nanoseconds, to be analyzed with fast-timing methods. The fast-timing method relies on measuring the time difference between a feeding and a depopulating transition of the state of interest. When one signal is given by the feeder of an intermediate state and the other one by the depopulating γ ray,

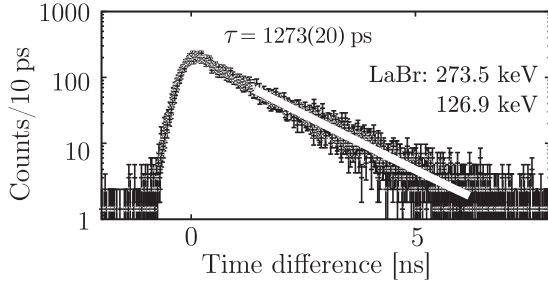


FIG. 4. Time-difference distribution obtained by a direct HPGe energy gate on the $6_1^+ \rightarrow 4_1^+$ transition, feeding the 4_1^+ state to clean the cascade of interest. The LaBr gates were applied to the $4_1^+ \rightarrow 2_1^+$ (273.5 keV) and the $2_1^+ \rightarrow 0_1^+$ (126.9 keV) transitions. The straight line represents the slope fit to the exponential part of the distribution.

the delayed time distribution is obtained [34]:

$$D(t) = n\lambda \int_{-\infty}^t \text{PRF}(t' - C_P) e^{-\lambda(t-t')} dt' + n_r, \quad \lambda = \frac{1}{\tau}, \quad (1)$$

where C_P corresponds to the centroid position of the prompt response function (PRF) of the timing system, n is the number of coincidences in the time distribution, n_r is the number of background counts, and τ is the lifetime of the state connected by the feeder-decay cascade. The delayed time distribution $D(t)$ is a convolution of the PRF of the system and an exponential decay.

The lifetime of the 2_1^+ state was analyzed using the well established slope method [35]. The lifetimes of the 4^+ and the 6^+ state both lie in the picosecond regime and were analyzed using the digital centroid shift method as described in Ref. [30].

A spectrum of the observed γ rays in coincidence with the $2_1^+ \rightarrow 0_1^+$ ground state transition for both detector groups (LaBr and HPGe) is depicted in Fig. 3. The transitions used for the lifetime analysis are indicated in red. The γ -ray spectrum shows the typical back-bending behavior of the γ rays between the states with $I = 10$ –16 [36]. This phenomenon is assumed to have an influence on the lifetime determination of the 6_1^+ state, because the feeding transition $8_1^+ \rightarrow 6_1^+$ is contaminated by the decays of the 16_1^+ and the 14_1^+ states. This will be addressed in Sec. III.

A. Lifetime of the first 2^+ state

The lifetime of the 2_1^+ state was analyzed using the slope method, and a plot of the time-difference distribution with the fitted exponential decay is presented in Fig. 4. The time-difference distribution was generated with a direct HPGe gate using the $6_1^+ \rightarrow 4_1^+$ (393.8 keV) transition, feeding the 4_1^+ state to select the cascade of interest. The LaBr gates were applied to the $4_1^+ \rightarrow 2_1^+$ (273.5 keV) and the $2_1^+ \rightarrow 0_1^+$ (126.9 keV) transitions. The total counts in the time-difference distribution amount to approximately $n = 25\,000$. The background level is approximately $n_r = 0.2/10$ ps. The lifetime amounts to $\tau = 1273(20)$ ps. The lifetime of the 2_1^+ state was previously reported with two disagreeing results of 1173(14) and 1370(144) ps [37,38]. The remeasured value here supports the

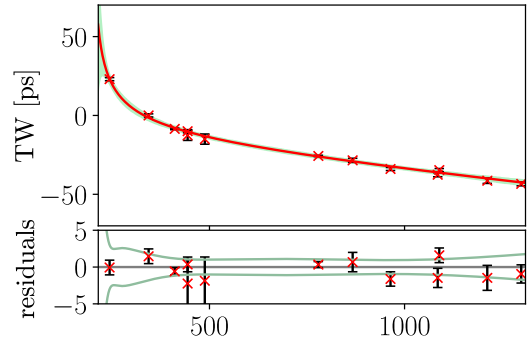


FIG. 5. Time walk calibration for the energy range between 240 and 1300 keV. The maximum time walk range is below 50 ps in the energy range under consideration. The uncertainty band in the lower plot represents the 1σ interval and is considered as the TW uncertainty throughout this work.

second one and an evaluation of all three values amounts in an adopted lifetime of $\tau = 1272(49)$ ps, which will be used for further discussion.

B. The centroid shift analyses

The lifetimes of the 4_1^+ and 6_1^+ states were analyzed using the centroid shift method [35] with the digital approach described in detailed in Ref. [30]. The lifetime is extracted from the centroid shift of the delayed time-difference distribution from the zero reference time T_0 of the timing system, and is given by

$$\tau = C_D - T_0 - \text{TW}(E_1, E_2), \quad (2)$$

where C_D corresponds to the centroid position of the delayed time-difference distribution, $T_0 = 0$ here and $\text{TW}(E_1, E_2)$ represents the energy-dependent time walk between the energies of the two involved transitions, which has to be calibrated for every timing system. The TW was calibrated using a standard ^{152}Eu calibration source, providing several γ -ray cascades connecting excited states with well known lifetimes [39] and the recently significantly improved lifetime for the 2_1^+ state of ^{152}Gd [40] of $\tau(2_1^+, ^{152}\text{Gd}) = 46.9(3)$ ps using the procedure detailed in Ref. [41]. The time walk curve in use is defined by

$$\text{TW}(E) = \frac{a}{\sqrt{E-b}} + c + dE, \quad (3)$$

where a , b , c , and d are the free fit parameters of the time walk function, which depend on the properties of the constant fraction discriminator, that is used as a time pick-off device. The time walk characteristic for the digital timing setup is illustrated in Fig. 5 and has a maximum TW range of around 50 ps in the energy range between 200 and 1300 keV. The time-correlated Compton background under the peak of interest was corrected according the considerations in Ref. [42], Sec. 3.3. The corrected centroid of the time-difference distribution of the full-energy peak (FEP) of interest is defined as [42]

$$C_{\text{FEP}} = C_{\text{exp.}} + \frac{t_{\text{cor.}}(E_1) + t_{\text{cor.}}(E_2)}{2}, \quad (4)$$

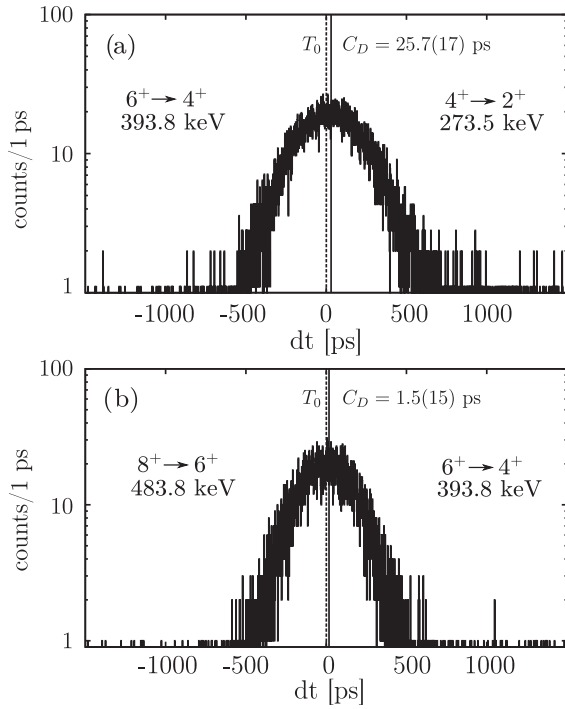


FIG. 6. (a) Time-difference distribution obtained with energy gates applied to the 2_1^+ state (127 keV) in HPGe detectors and to the 6_1^+ state (393.8 keV) and 4_1^+ state (273.5 keV) in LaBr detectors. (b) Time-difference distribution obtained with energy gates applied to the 2_1^+ state (126.9 keV) in HPGe detectors and to the 8_1^+ state (483.8 keV) and 6_1^+ state (393.8 keV) in LaBr detectors. In both plots, the centroid position C_D and the time reference of the system T_0 are indicated and the energy gates applied to the LaBr detectors are provided.

where the background time correction term is given as [42]

$$t_{\text{cor.}} = \frac{C_{\text{exp.}} - C_{\text{BG}}}{p/b}. \quad (5)$$

The quantity p/b corresponds to the ratio of the counts in the FEP to the counts in the background of the energy gate that is used to generate the experimental time-difference distribution.

1. Lifetime of the first 4^+ state

An exemplary time-difference distribution for the determination of the lifetime of the 4_1^+ state containing the full experimental statistics after a HPGe gate on the $2_1^+ \rightarrow 0_1^+$ (126.9 keV) transition and two LaBr gates on the $6_1^+ \rightarrow 4_1^+$ (393.8 keV) and $4_1^+ \rightarrow 2_1^+$ (273.5 keV) transitions is depicted in Fig. 6(a). The system zero time reference $T_0 = 0$ and the centroid position C_D are indicated in the plot. The lifetime was determined using two different HPGe gates to select the γ cascade of interest: one on the $2_1^+ \rightarrow 0_1^+$ (126.9 keV) transition, the other on the $8_1^+ \rightarrow 6_1^+$ (483.8 keV) transition. In Fig. 7, a gated energy spectrum of the region around the $4_1^+ \rightarrow 2_1^+$ transition (a) and the time-correlated background correction procedure (b) are exemplarily illustrated for a HPGe gate on the $2_1^+ \rightarrow 0_1^+$ transition. The centroid position C_D obtained lies at $C_D = 25.7(17)$ ps (depending on the

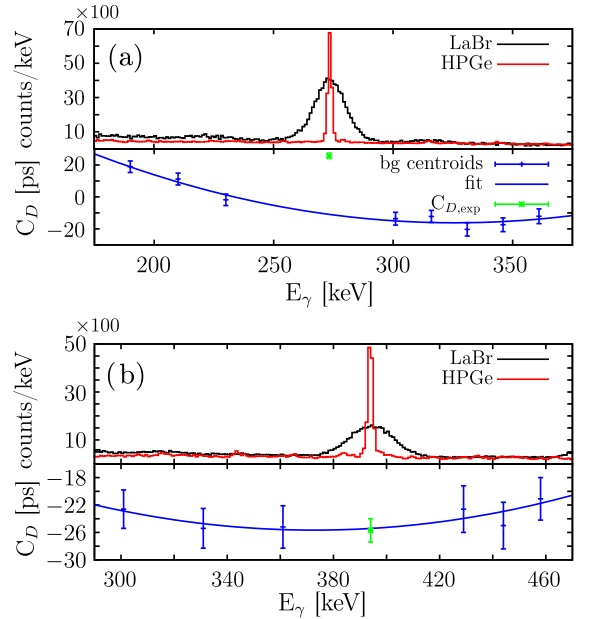


FIG. 7. Exemplary lifetime analysis and background correction for the 4_1^+ state. (a) LaBr spectrum and HPGe reference spectrum with energy gates applied to the $2_1^+ \rightarrow 0_1^+$ (127 keV) transition in HPGe detectors and to the $6_1^+ \rightarrow 4_1^+$ (393.8 keV) transition in LaBr detectors. The lower part of the figure shows the background correction procedure for the $4_1^+ \rightarrow 2_1^+$ transition. The centroid positions taken in the background around the peak of interest and the fit are depicted in blue. The experimental centroid position $C_{D,\text{exp}}$ is indicated in green. (b) LaBr spectrum and HPGe reference spectrum with energy gates applied to the 2_1^+ state (127 keV) in HPGe detectors and to the $4_1^+ \rightarrow 2_1^+$ (273.5 keV) transition in LaBr detectors. The lower part of the figure shows the background correction procedure for the $6_1^+ \rightarrow 4_1^+$ transition. The centroid positions taken in the background around the peak of interest and the fit are depicted in blue.

triggering HPGe gate). The time walk between the involved γ energies amounts to $\text{TW}(393.8 \text{ keV}, 273.5 \text{ keV}) = -18.3(8)$ ps. The peak-to-background ratios amount to $p/b_{273.5 \text{ keV}} = 4.3(1)$ and $p/b_{393.8 \text{ keV}} = 3.3(1)$. The individual lifetime values obtained from the different HPGe gates agree within the uncertainties and an adopted lifetime of $\tau = 48.1(14)$ ps is obtained using a Monte Carlo uncertainty propagation. The results are summarized in Table I.

2. Lifetime of the first 6^+ state

The lifetime of the 6^+ state was determined using the timing cascade $8_1^+ \rightarrow 6_1^+ \rightarrow 4_1^+$ (483.8–393.8 keV) and two different HPGe gates to select the γ -cascade of interest on $2_1^+ \rightarrow 0_1^+$ (127 keV) and $4_1^+ \rightarrow 2_1^+$ (273 keV). All analyses were carried out according to that of the lifetime of the 4_1^+ state. Figure 6(b) shows an exemplary time-difference distribution of the energy gate sequence $8_1^+ \rightarrow 6_1^+ \rightarrow 4_1^+ \rightarrow 2_1^+$ with energy gates on LaBr-LaBr-HPGe, respectively. $T_0 = 0$ and the centroid position C_D are indicated in the plot. The time-correlated background correction was applied similarly to the background correction of the lifetime of the 4_1^+ state. The time walk between the involved transition energies

TABLE I. Summary of lifetimes measured in this work and derived reduced transition strengths in comparison to literature values and IBM-1 calculations from this work; see Sec. IV. The lifetime values printed in bold are obtained from a Monte Carlo uncertainty propagation and adopted for further discussion and the extraction of the $B(E2)$ values. The lifetime value for the 2_1^+ state is obtained from a Monte Carlo uncertainty propagation of the newly determined value and the two literature values.

I^π	HPGe gate	τ (ps)		$B(E2)$ ($10^{-2} e^2 b^2$)		
		This work	Lit.	This work	Lit.	IBM-1
2_1^+	$6_1^+ \rightarrow 4_1^+$	1273(20)	1173(16) ^a 1370(144) ^b		76.8(13) 66(8)	
		1272(49)		71(3)		71
4_1^+	$2_1^+ \rightarrow 0_1^+$	48.7(21)				
	$8_1^+ \rightarrow 6_1^+$	47.5(17)				
		48.1(14)		99(3)		101
6_1^+	$2_1^+ \rightarrow 0_1^+$	8.4(18)				
	$4_1^+ \rightarrow 2_1^+$	7.9(18)				
		8.1(12)		102^{+33}_{-13}		110

^aReference [37].

^bReference [38].

amounts to $TW(483.8 \text{ keV}, 393.8 \text{ keV}) = -6.3(5)$ ps. The centroid position is about $C_D = 1.5(15)$ ps (depending on the HPGe gate) and the peak-to-background ratios amount to $p/b_{393.8 \text{ keV}} = 4.0(2)$ and $p/b_{483.8 \text{ keV}} = 4.0(1)$. The individual lifetime values depending on the HPGe gates agree within the uncertainties. The lifetime of $\tau = 8.1(12)$ ps is obtained for the 6_1^+ state using a Monte Carlo uncertainty propagation. The previously mentioned 14_1^+ and 16_1^+ decays due to the back-bending phenomenon contaminate the lifetime analysis of the 6_1^+ state. The contaminating peaks at 495 keV ($14_1^+ \rightarrow 12_1^+$) and 479 keV ($16_1^+ \rightarrow 14_1^+$) have an intensity of around 10% of the $8_1^+ \rightarrow 6_1^+$ transition for both contaminating transitions. Efforts were made to minimize the impact of potential contamination through the use of narrow gates on the 483.8 keV transition and the background correction, although it is possible that the lifetime is still a bit overestimated. Hence, the negative uncertainty is extended about 0.8 ps, which corresponds to another 10%. Hence, the adopted lifetime amounts to $\tau = 8.1_{-2}^{+1.2}$ ps.

All individual and adopted lifetimes are summarized in Table I alongside with deduced $B(E2)$ values (see Sec. IV) and $B(E2)$ values from IBM-1 calculations (see Sec. IV).

IV. DISCUSSION

The neutron-midshell region of interest (see Fig. 1) is well characterized in most of the signatures important for quadrupole deformation of nuclei. Especially, the osmium isotopic chain provides one of the longest chains with consecutively known spectroscopic data for even-even isotopes on the entire chart of nuclei [11]. All $R_{4/2}$ ratios as well as all $B(E2; 2^+ \rightarrow 0^+)$ values and most of the $B_{4/2}$ values with the notable exception of $^{176,182}\text{Os}$ are known for the even-even isotopes of the W, Os, Pt, and Hg isotopic chains around neutron midshell, $N = 104$ [11]; see Fig. 2. The previously

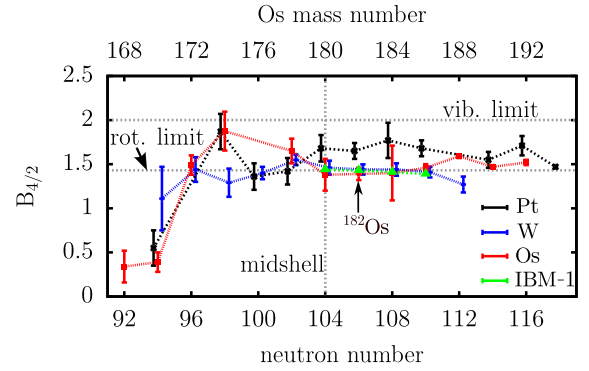


FIG. 8. $B_{4/2}$ ratios for the osmium, platinum, and tungsten isotopic chains. The newly determined value of $^{182}\text{Os}_{106}$ is indicated by a dashed box. The orange triangles represent the results of the IBM-1 calculations; see Sec. IV. The dashed lines connecting the data points are meant to guide the eyes. The theoretical limits of ideal rotors and vibrators as well as the neutron midshell are shown with grey dashed lines. The values for $^{172,176,180}\text{Pt}$, $^{176,178,180}\text{W}$, and $^{168,172,174,178}\text{Os}$ are taken from Refs. [7,17,27–29]. All other values taken from nuclear data sheets [11].

unknown $B_{4/2}$ ratio of ^{182}Os was determined in this work and amounts to 1.39(7). Within the uncertainties, this value agrees with the rotational limit of 1.43 (see Fig. 8). As Fig. 8 shows, the $B_{4/2}$ ratios of the neighboring osmium and tungsten isotopes also stick close to the rotor limit. The $B_{4/2}$ ratios of neighboring platinum exhibit a slight increase towards the vibrational limit. As suggested by the $R_{4/2}$ ratio of ^{182}Os of 3.15, the $B_{4/2}$ ratio of 1.39(7) allows for an interpretation as a rigid, quadrupole deformed rotor [19,20]. The absolute value for the quadrupole deformation β_2 was recalculated using the rotational model based on the adopted value of the lifetime of the 2_1^+ state and amounts to 0.22(4). The quadrupole deformation of the 4_1^+ state also amounts to 0.22(2) and the one of the 6_1^+ state amounts to 0.21(8). This corresponds to a moderate quadrupole deformation throughout all measured states of ^{182}Os [18].

Still, some peculiarities are observed in ^{182}Os : A possible change in structure of higher excitation bands is taking place at the neutron number $N = 106$ or the neighboring $N = 107$ isotope. The excitation energies of the lowest yrast states exhibit an expected trend, as demonstrated by Fig. 9(a), with a minimum value observed close to the neutron midshell at $N = 104$. However, the excitation energies of the 2_2^+ and 0_2^+ states indicate a departure from the previously observed trends in the isotopic chain close to or at $^{182}\text{Os}_{106}$, respectively.

The energies of the 2_2^+ state, which serves as the bandhead of the γ -rotational band in most osmium isotopes, are around 900 keV for the lighter osmium isotopes ($96 < N < 108$) with a maximum at $^{184}\text{Os}_{108}$. As more neutrons are added, the γ -band energies exhibit a sharp break and a beginning even-odd staggering behavior, indicating the emergence of γ softness around $^{184-192}\text{Os}$ [12–15,43]. At $N = 114$, $E_{4_1^+}$ and $E_{2_2^+}$ intersect and are almost equal, which is an indication of γ -soft nuclei [44] (and also vibrational structures, which is, however, not expected in this context at all). The excitation energies of the 0_2^+ state perform an opposite movement: the

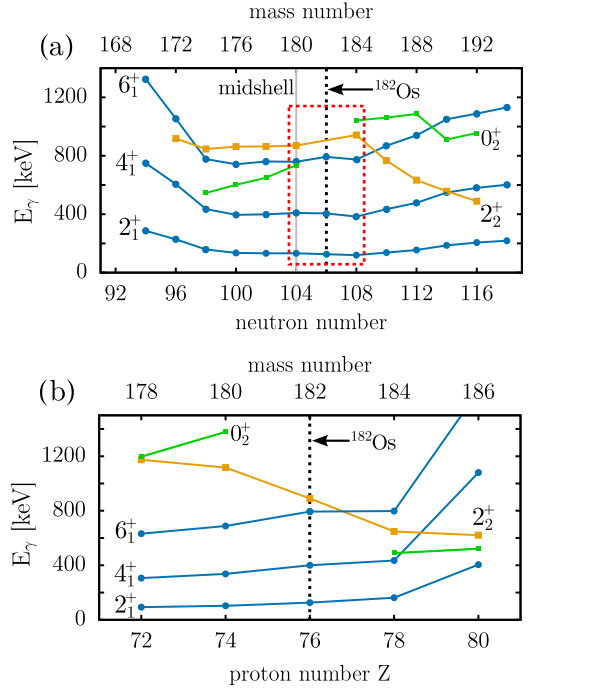


FIG. 9. (a) Evolution of level energies of the osmium isotopes around neutron midshell, $N = 104$. The red dashed box marks the area of interest. The blue dots represent the level energies of the 2_1^+ , 4_1^+ , 6_1^+ states of the ground state band. The orange squares are the energies of the 2_2^+ states and the green squares are the energies of the 0_2^+ state. (b) Energies of the first three yrast states and 2_2^+ and 0_2^+ states versus proton number Z of the isotones with $N = 106$. The lines connecting the data points are meant to guide the eyes. All values are taken from [11].

$E_{0_2^+}$ for the osmium isotopes with $N = 108, 110, 112$ are observed to be around 1000 keV, but decrease to below 800 keV for ^{180}Os and lower as neutrons are removed. In particular, no 0_2^+ state has been previously reported for ^{182}Os at all. The drop in $E_{0_2^+}$ is an indication of the emergence of the X(5) critical point symmetry in the lighter osmium isotopes $^{176,178}\text{Os}$, where $E_{6_1^+}$ and $E_{0_2^+}$ are expected to be degenerate [45]. From this point of view, ^{182}Os is suggested as a transition point between the fading influence of the γ softness, where $E_{0_2^+}$ lies above $E_{2_2^+}$ [44], in the heavier isotopes and the X(5) symmetry in the lighter isotopes. Figure 9(b) shows the evolution of the same states as in Fig. 9(a) but along the isotonic chain with $N = 106$, at the end of which is ^{186}Hg , where a weakly oblate-deformed ground state band coexists with a prolate intruder band in low-spin states [4,46]. The yrast band structure rises as expected, when approaching a closed shell. But as evidenced by the dropping excitation energies of the 0_2^+ and 2_2^+ states, also from the isotonic perspective ^{182}Os might represent a transition point between the prevailing prolate deformation from proton-deficient isobars and the dominating shape coexistence characteristic when adding protons.

These depicted discontinuities, however, do not influence the lower excited yrast states of ^{182}Os , and this nucleus can be considered the first in the $N = 106$ isotonic chain to show distinct rotor signs. The strongly deformed rare-earth region

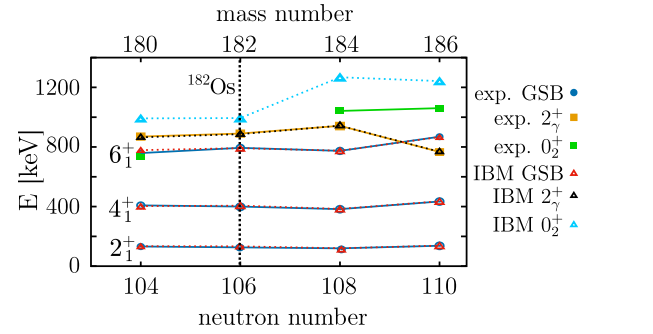


FIG. 10. Experimental and theoretical level energies of first three ground state band states and 2_2^+ and 0_2^+ states of $^{180-186}\text{Os}$. IBM values are illustrated with triangles of different colors. The theoretical values for the ground state bands and the 2_2^+ states are taken from Ref. [12]. The theoretical values for the 0_2^+ states were calculated in the scope of this paper. The lines are meant to guide the eyes.

far from the closed shells finds an edge here, as the ^{184}Pt yet deviates from the rotor limits in $R_{4/2}$ and $B_{4/2}$ signatures and $E_{2_2^+}$ and $E_{0_2^+}$.

Interacting boson model 1 (IBM-1) [21] calculations were made based on calculations of Sogunlu and van Isacker [12] for the isotopes $^{180-186}\text{Os}$, where the calculations including a Hamiltonian and fit parameters are detailed. In Ref. [12], the ground state band energies up to $I = 10$ and γ -band energies up to the least known $I = 6-10$ were fitted. The energies of the 0_2^+ state were additionally calculated here. The level energies of the yrast band and the γ band are reproduced with root mean square deviations of $\sigma = 5-19$ keV for all calculated levels, as Fig. 10 illustrates. The results of the calculations reproduce the discontinuities regarding the level energies of 2_2^+ and 0_2^+ . The level energies of the 0_2^+ state are overestimated by the model. However, the jump of the theoretical values of $E_{0_2^+}$ between ^{182}Os and ^{184}Os are reproduced, as depicted in Fig. 10. Figure 8 shows that the calculated $B_{4/2}$ values are well reproduced for the isotopes $^{180-186}\text{Os}$, including the newly determined $B_{4/2}$ of ^{182}Os . It places the $B_{4/2}$ value close to the rotational limit of ≈ 1.43 and agrees with the experimental value within its uncertainties. This calculation shows that the IBM-1 in a simple form, as used here, is excellently able to describe the rotors with boson numbers from 11 to 14 at the edge of the collective region with $A \approx 180$.

V. CONCLUSION

Lifetimes of the first excited 4^+ and 6^+ states in ^{182}Os have been measured for the first time and amount to $\tau_{4^+} = 48.1(14)$ ps and $\tau_{6^+} = 8.1(12)$ ps. The lifetime of the first excited 2^+ state has been remeasured with high precision and supports one of the previously measured literature values. The evaluated lifetime between all three values obtained by Monte Carlo uncertainty propagation amounts to $\tau_{2^+} = 1272(49)$ ps and was adopted for further discussions. With the newly determined and evaluated lifetimes, the $B(E2)$ values between the 6_1^+ , 4_1^+ , and 2_1^+ states and corresponding deformation parameters β_2 were extracted. A $B_{4/2}$ value of $1.39(7)$ of ^{182}Os was determined and classified in the context

of the neighboring isotopes. In accordance with IBM-1 calculations the collective and rotorlike structure is suggested by the $B_{4/2}$ value, as expected from the already known collective signatures. ^{182}Os marks the edge of the strongly deformed rare-earth region in the $N = 106$ isotonic chain as ^{184}Pt cannot serve with clear collective signs. Still, ^{182}Os shows transitional behavior in higher lying excitation bands between the heavier γ -soft and the lighter X(5) candidates in the osmium isotopes and the strongly deformed rotors in the lighter isotones, e.g., tungsten and hafnium, and the onset of coexisting shapes in low excitation levels of the heavier isotones platinum and mercury. Further lifetime measurements of the higher yrast states and the 2_2^+ state potentially with the recoil-distance Doppler shift method and the subsequent $B(E2)$ values as

well as spectroscopic measurements to potentially discover a $K^\pi = 0^+$ band can provide more clarity about the onset of the shape coexistence phenomena and slight γ softness in ^{182}Os .

ACKNOWLEDGMENTS

The authors would like to thank the operator staff of the FN Tandem accelerator at the Institut für Kernphysik, Cologne. M.L. acknowledges the Deutsche Forschungsgemeinschaft (DFG) for support under Grant No. JO 391/18-1. A.E. wants to acknowledge the support of BMBF Verbundprojekt 05P2021 (ErUM-FSP T07) under Grant No. 05P21PKFN1. We acknowledge the DFG for the upgrade of the used German detectors under grant INST 216/988-1 FUGG.

-
- [1] D. T. Joss, S. L. King, R. D. Page, J. Simpson, A. Keenan, N. Amzal, T. Bäck, M. A. Bentley, B. Cederwall, J. F. C. Cocks, D. M. Cullen, P. T. Greenlees, K. Helariutta, P. M. Jones, R. Julin, S. Juutinen, H. Kankaanpää, H. Kettunen, P. Kuusiniemi, M. Leino *et al.*, *Nucl. Phys. A* **689**, 631 (2001).
- [2] M. C. Drummond, D. T. Joss, R. D. Page, J. Simpson, D. O'Donnell, K. Andgren, L. Bianco, B. Cederwall, I. G. Darby, S. Eeckhauht, M. B. Gomez-Hornillos, T. Grahn, P. T. Greenlees, B. Hadinia, P. M. Jones, R. Julin, S. Juutinen, S. Ketelhut, A.-P. Leppänen, M. Leino *et al.*, *Phys. Rev. C* **87**, 054309 (2013).
- [3] D. T. Joss, K. Lagergren, D. E. Appelbe, C. J. Barton, J. Simpson, B. Cederwall, B. Hadinia, R. Wyss, S. Eeckhauht, T. Grahn, P. T. Greenlees, P. M. Jones, R. Julin, S. Juutinen, H. Kettunen, M. Leino, A.-P. Leppänen, P. Nieminen, J. Pakarinen, P. Rakkila *et al.*, *Phys. Rev. C* **70**, 017302 (2004).
- [4] K. Heyde and J. L. Wood, *Rev. Mod. Phys.* **83**, 1467 (2011).
- [5] G. Häfner, A. Esmaylzadeh, J. Jolie, J.-M. Régis, C. Müller-Gatermann, A. Blazhev, C. Fransen, R.-B. Gerst, V. Karayonchev, L. Knafla, N. Saed-Samii, and K.-O. Zell, *Eur. Phys. J. A* **57**, 5 (2021).
- [6] A. Dewald, O. Möller, B. Melon, T. Pissulla, B. Saha, S. Heinze, J. Jolie, K. O. Zell, P. Petkov, D. Bazzacco, S. Lunardi, C. A. Ur, E. Farnea, R. Menegazzo, G. De Angelis, D. Tonev, D. R. Napoli, N. Marginean, T. Martinez, M. Axiotis *et al.*, in *Frontiers in Nuclear Structure, Astrophysics, and Reactions - FINUSTAR*, 12–17 September 2005, Isle of Kos, Greece, edited by S. V. Harissopulos P. Demetriou, and R. Julin, AIP Conf. Proc. No. 831 (AIP, New York, 2006), p. 195.
- [7] A. Harter, L. Knafla, G. Frießner, G. Häfner, J. Jolie, A. Blazhev, A. Dewald, F. Dunkel, A. Esmaylzadeh, C. Fransen, V. Karayonchev, K. Lawless, M. Ley, J.-M. Régis, and K. O. Zell, *Phys. Rev. C* **106**, 024326 (2022).
- [8] J. Wiederhold, V. Werner, R. Kern, N. Pietralla, D. Bucurescu, R. Carroll, N. Cooper, T. Daniel, D. Filipescu, N. Florea, R.-B. Gerst, D. Ghita, L. Gurgi, J. Jolie, R. S. Ilieva, R. Lica, N. Marginean, R. Marginean, C. Mihai, I. O. Mitu *et al.*, *Phys. Rev. C* **99**, 024316 (2019).
- [9] M. Rudigier, K. Nomura, M. Dannhoff, R.-B. Gerst, J. Jolie, N. Saed-Samii, S. Stegemann, J.-M. Régis, L. M. Robledo, R. Rodríguez-Guzmán, A. Blazhev, C. Fransen, N. Warr, and K. O. Zell, *Phys. Rev. C* **91**, 044301 (2015).
- [10] P. J. R. Mason, Z. Podolyák, N. Märginean, P. H. Regan, P. D. Stevenson, V. Werner, T. Alexander, A. Algora, T. Alharbi, M. Bowry, R. Britton, A. M. Bruce, D. Bucurescu, M. Bunce, G. Căta-Danil, I. Căta-Danil, N. Cooper, D. Deleanu, D. Delion, D. Filipescu *et al.*, *Phys. Rev. C* **88**, 044301 (2013).
- [11] Evaluated nuclear structure data file (ensdf), online database, accessed on 2023-03-31.
- [12] B. Sorgunlu and P. Van Isacker, *Nucl. Phys. A* **808**, 27 (2008).
- [13] C. Wheldon, G. Dracoulis, R. Newman, P. Walker, C. Pearson, A. Byrne, A. Baxter, S. Bayer, T. Kibédi, T. McGoram, S. Mullins, and F. Xu, *Nucl. Phys. A* **699**, 415 (2002).
- [14] P. Bond, R. Casten, D. Warner, and D. Horn, *Phys. Lett. B* **130**, 167 (1983).
- [15] P. R. John, V. Modamio, J. J. Valiente-Dobón, D. Mengoni, S. Lunardi, T. R. Rodríguez, D. Bazzacco, A. Gadea, C. Wheldon, T. Alexander, G. de Angelis, N. Ashwood, M. Barr, G. Benzoni, B. Birkenbach, P. G. Bizzeti, A. M. Bizzeti-Sona, S. Bottoni, M. Bowry, A. Bracco *et al.*, *Phys. Rev. C* **90**, 021301 (2014).
- [16] Z. Podolyák, S. J. Steer, S. Pietri, F. R. Xu, H. L. Liu, P. H. Regan, D. Rudolph, A. B. Garnsworthy, R. Hoischen, M. Górska, J. Gerl, H. J. Wollersheim, T. Kurtukian-Nieto, G. Benzoni, T. Shizuma, F. Becker, P. Bednarczyk, L. Caceres, P. Doornenbal, H. Geissel *et al.*, *Phys. Rev. C* **79**, 031305 (2009).
- [17] O. Möller, Ph.D. thesis, Universität zu Köln, 2005.
- [18] R. F. Casten, *Nuclear Structure from a Simple Perspective*, Oxford Studies in Nuclear Physics Vol. 23 (Oxford University Press, Oxford, 2000).
- [19] A. Bohr and B. R. Mottelson, *Nuclear Structure: Vol. 1* (World Scientific, Singapore, 1969).
- [20] A. Bohr and B. R. Mottelson, *Nuclear Structure: Vol. 2* (World Scientific, Singapore, 1975).
- [21] A. Arima and F. Iachello, in *Advances in Nuclear Physics, Vol. 13*, edited by J. W. Negele and E. Vogt (Springer, New York, 2012), p. 139.
- [22] E. C. Simpson, *J. Phys.: Conf. Ser.* **1643**, 012168 (2020).
- [23] C. M. Baglin, *Nucl. Data Sheets* **111**, 275 (2010).
- [24] E. McCutchan, *Nucl. Data Sheets* **126**, 151 (2015).
- [25] R. Kaczarowski, U. Garg, A. Chaudhury, E. G. Funk, J. W. Mihelich, D. Frekers, R. V. F. Janssens, and T. L. Khoo, *Phys. Rev. C* **41**, 2069 (1990).

- [26] S. Raman, C. W. Nestor, and P. Tikkanen, *At. Data Nucl. Data Tables* **78**, 1 (2001).
- [27] B. Cederwall, M. Doncel, O. Aktas, A. Ertoprak, R. Liotta, C. Qi, T. Grahn, D. M. Cullen, B. S. Nara Singh, D. Hodge, M. Giles, S. Stolze, H. Badran, T. Braunroth, T. Calverley, D. M. Cox, Y. D. Fang, P. T. Greenlees, J. Hilton, E. Ideguchi *et al.*, *Phys. Rev. Lett.* **121**, 022502 (2018).
- [28] T. Grahn, S. Stolze, D. T. Joss, R. D. Page, B. Saygi, D. O'Donnell, M. Akmalı, K. Andgren, L. Bianco, D. M. Cullen, A. Dewald, P. T. Greenlees, K. Heyde, H. Iwasaki, U. Jakobsson, P. Jones, D. S. Judson, R. Julin, S. Juutinen, S. Ketelhut *et al.*, *Phys. Rev. C* **94**, 044327 (2016).
- [29] A. Goasduff, J. Ljungvall, T. R. Rodríguez, F. L. Bello Garrote, A. Etile, G. Georgiev, F. Giacompo, L. Grente, M. Klintefjord, A. Kuşoğlu, I. Matea, S. Roccia, M.-D. Salsac, and C. Sotty, *Phys. Rev. C* **100**, 034302 (2019).
- [30] A. Harter, M. Weinert, L. Knafla, J.-M. Régis, A. Esmaylzadeh, M. Ley, and J. Jolie, *Nucl. Instrum. Methods Phys. Res., Sect. A* **1053**, 168356 (2023).
- [31] L. Knafla, G. Häfner, J. Jolie, J.-M. Régis, V. Karayonchev, A. Blazhev, A. Esmaylzadeh, C. Fransen, A. Goldkuhle, S. Herb, C. Müller-Gatermann, N. Warr, and K. O. Zell, *Phys. Rev. C* **102**, 044310 (2020).
- [32] A. Esmaylzadeh, L. M. Gerhard, V. Karayonchev, J.-M. Régis, J. Jolie, M. Bast, A. Blazhev, T. Braunroth, M. Dannhoff, F. Dunkel, C. Fransen, G. Häfner, L. Knafla, M. Ley, C. Müller-Gatermann, K. Schomacker, N. Warr, and K.-O. Zell, *Phys. Rev. C* **98**, 014313 (2018).
- [33] V. Karayonchev, A. Blazhev, A. Esmaylzadeh, J. Jolie, M. Dannhoff, F. Diel, F. Dunkel, C. Fransen, L. M. Gerhard, R.-B. Gerst, L. Knafla, L. Kornwebel, C. Müller-Gatermann, J.-M. Régis, N. Warr, K. O. Zell, M. Stoyanova, and P. Van Isacker, *Phys. Rev. C* **99**, 024326 (2019).
- [34] Z. Bay, *Phys. Rev.* **77**, 419 (1950).
- [35] H. Mach, R. Gill, and M. Moszyński, *Nucl. Instrum. Methods Phys. Res., Sect. A* **280**, 49 (1989).
- [36] K. S. Krane, D. Halliday *et al.*, *Introductory Nuclear Physics*, (John Wiley & Sons, New York, 1988).
- [37] R. Broda, J. Golczewski, A. Z. Hryniewicz, R. Kulesza, and W. Walus JINR Technical Report No. JINR-E6-5070, 1970 (unpublished).
- [38] B. R. Erdal, M. Finger, R. Foucher, J. P. Husson, J. Jastrzebski, A. Johnson, N. Perrin, R. Henck, R. Regal, P. Siffert, G. Astner, A. Kjelberg, P. Patzelt, A. Hoglund, and S. Malmskog, in Proceedings of International Conference on Properties of Nuclei far from the Region of Beta-Stability, 1970 (unpublished).
- [39] M. Martin, *Nucl. Data Sheets* **114**, 1497 (2013).
- [40] L. Knafla, A. Harter, M. Ley, A. Esmaylzadeh, J.-M. Régis, D. Bittner, A. Blazhev, F. von Spee, and J. Jolie, *Nucl. Instrum. Methods Phys. Res., Sect. A* **1052**, 168279 (2023).
- [41] J.-M. Régis, N. Saed-Samii, M. Rudigier, S. Ansari, M. Dannhoff, A. Esmaylzadeh, C. Fransen, R.-B. Gerst, J. Jolie, V. Karayonchev, C. Müller-Gatermann, and S. Stegemann, *Nucl. Instrum. Methods Phys. Res., Sect. A* **823**, 72 (2016).
- [42] J.-M. Régis, M. Dannhoff, and J. Jolie, *Nucl. Instrum. Methods Phys. Res., Sect. A* **897**, 38 (2018).
- [43] X. Q. Yang, L. J. Wang, J. Xiang, X. Y. Wu, and Z. P. Li, *Phys. Rev. C* **103**, 054321 (2021).
- [44] R. Casten, P. Von Brentano, K. Heyde, P. Van Isacker, and J. Jolie, *Nucl. Phys. A* **439**, 289 (1985).
- [45] F. Iachello, *Phys. Rev. Lett.* **87**, 052502 (2001).
- [46] L. P. Gaffney, M. Hackstein, R. D. Page, T. Grahn, M. Scheck, P. A. Butler, P. F. Bertone, N. Bree, R. J. Carroll, M. P. Carpenter, C. J. Chiara, A. Dewald, F. Filmer, C. Fransen, M. Huyse, R. V. F. Janssens, D. T. Joss, R. Julin, F. G. Kondev, P. Nieminen *et al.*, *Phys. Rev. C* **89**, 024307 (2014).